Nanoscale

ROYAL SOCIETY OF CHEMISTRY

PAPER

View Article Online
View Journal | View Issue

Cite this: *Nanoscale*, 2024, **16**, 645

Fabrication of a tough, long-lasting adhesive hydrogel patch *via* the synergy of interfacial entanglement and adhesion group densification†

Yunjie Lu, Zhaohui Li, Zewei Li, Shihao Zhou, Ning Zhang, Jianming Zhang and Lu Zong *

Adhesive hydrogels (AHs) are considered ideal materials for flexible sensors. However, the lack of effective energy dissipation networks and sparse surface polar groups in AHs lead to poor mechanical properties and interfacial adhesion, which limit their practical application. Herein, a tough, long-lasting adhesive and highly conductive nanocomposite hydrogel (PACPH) was fabricated *via* the synergy of interfacial entanglement and adhesion group densification. PACPH was obtained by the *in situ* polymerization of highly carboxylated cellulose nanocrystals (SCNCPA, surface pre-grafted polyacrylic acid chains, C_{-COOH} = 11.5 mmol g^{-1}) with the acrylic acid precursor. The unique tacticity of SCNCPA provides strong interface entanglement and multiple hydrogen bonds with the PACPH network, which further increases the energy dissipated during SCNCPA displacements, and enhances the mechanical properties of PACPH (tensile strength = 1.45 MPa, modulus = 332 kPa, and fracture toughness = 13.2 MJ m^{-3}). Meanwhile, SCNCPA increases the density of surface polar groups in PAPCH and also acts as an anchor point to improve the adhesion strength (>2–3 times) of PACPH on various substrates. The combination of excellent mechanical, adhesive, and conductive properties of the PAPCH-integrated patches enables long-term monitoring of human daily activities and electrocardiogram (ECG) signals, verifying that PAPCH is a promising material platform for the further development of flexible sensors and other health management devices.

Received 8th October 2023,
Accepted 30th November 2023

DOI: 10.1039/d3nr05049a

rsc.li/nanoscale

Introduction

Hydrogels are a kind of soft material composed of a three-dimensional network structure and a large amount of water; they exhibit good biocompatibility with and strong performance suitability for human tissues, which have broaden their application prospects in the fields of healthcare, soft robotics, and virtual interactive experience devices.[1] The emergence of adhesive hydrogels (AHs) has further accelerated the development of hydrogel applications, such as antipyretic patches, medical electrode patches, and brain interface patches, which have gradually entered our lives.[2] However, there are still some problems in the application of AHs. Firstly, a majority of AHs have a simple network structure and do not exhibit effective energy dissipation during deformation, leading to poor mechanical properties, large deformation ability and low modulus (10–100 kPa).[3] Undoubtedly, the occurrence of large deformation or even fracture under a small stress is disastrous. Secondly, the presence of a large amount of water in AHs results in a low density of polar groups on the surface; fewer effective links at the adhesion interface with the substrate lead to a low adhesion force, which along with the limitation of its own strength can easily lead to interfacial de-adhesion and functional failure (*e.g.* sensing interruption).[4] Finally, in practi-

Key Laboratory of Rubber-Plastics, Ministry of Education/Shandong Provincial Key Laboratory of Rubber-Plastics, Qingdao University of Science & Technology, Qingdao City 266042, People's Republic of China. E-mail: zonglu@qust.edu.cn

† Electronic supplementary information (ESI) available. See DOI: https://doi.org/10.1039/d3nr05049a

Lu Zong

Lu Zong is an Associate Professor at the School of Polymer Science and Engineering at the Qingdao University of Science and Technology. He received his PhD in material science from the University of Chinese Academy of Sciences in 2018. His research focuses on biomass-based hybrid materials and their nanocomposites for application in functional hydrogels, soft robotics, actuators and sensors.

cal applications, the synergy of excellent mechanical and adhesion properties is urgently needed to develop AHs with a long-lasting and stable sensing performance.[5]

Nanocomposite construction is an effective strategy to toughen hydrogels, and a considerable number of studies have demonstrated that the nanomaterials in composite hydrogels can effectively dissipate energy.[6,7] For example, inorganic nanomaterials, such as MXenes,[8] carbon nanotubes (CNTs)[9] and graphene (GO),[10] have been used to prepare nanocomposite hydrogels by simple mixing. Shen *et al.* reported nanocomposite hydrogels prepared by the one-pot radical polymerization of 3-acrylamidophenylboronic acid and acrylamide in the presence of stably dispersed CNTs.[9] The rigid CNTs could dissipate some of the energy during deformation, enhancing the mechanical properties of the composite hydrogel (the tensile strength, modulus and fracture energy values reaching 323 kPa, 50 kPa and 1078 J m^{-2}, respectively). However, nanomaterials, such as CNTs, GO and MXenes, are limited by their own structure; their low surface charge density results in poor dispersion in the hydrogel, and hence they need to be dispersed with assistance. On the other hand, their interactions with the hydrogel molecular chain network are low, and the support they provide in energy dissipation is also limited.[11] In addition, the low surface charge density of these nanomaterials has little effect on the adhesion of the hydrogel, and the addition of these nanomaterials tends to have a significant impact on some of the properties of the hydrogel (optical properties, for instance).[12]

Recently, biomass nanomaterials, such as cellulose nanocrystals (CNC) and nanofibers (CNF), have attracted a lot of attention from researchers due to their high modulus, low density, and biocompatibility.[13,14] In particular, using surface modification treatments, such as TEMPO oxidation and surface grafting, the surfaces of these materials can be given a variety of designs to meet specific needs.[15] For example, CNCs or CNFs can obtain a certain amount of –COOH groups (2–4 mmol g^{-1}) on their surface after TEMPO treatment, which is beneficial for better dispersion and improves the interaction with the hydrogel molecular chain network (hydrogen bonds and chain entanglement).[16] Qin *et al.* prepared a high-performance perspiration sensor (CPPH) by a one-pot method using a uniform blend of TOCNF, borax, polyaniline, and polyvinyl alcohol (PVA) precursors.[17] The carboxylate structure on the surface of the TOCNF not only promoted its uniform dispersion but also enhanced the non-covalent interactions (hydrogen bonding, *etc.*) between TOCNF and the PVA molecular chain network, which resulted in favourable mechanical properties. Similarly, Yao *et al.* prepared a nanocomposite hydrogel with excellent properties using carboxylated CNF (C-CNF) as a nano-filler.[18] After the carboxylation of CNF, the carboxyl groups on the surface provided strong interactions (hydrogen bonding and chain entanglement) with the hydrogel molecular chain network, resulting in excellent mechanical properties of the composite hydrogel (tensile strength 0.35 MPa, modulus 75 kPa, elongation at break 1800%). It is noteworthy that the addition of C-CNF also enhanced the adhesion properties of the composite hydrogel (23.7 kPa), which indicates that the carboxyl groups could not only enhance the interactions between the nanomaterials and the hydrogel molecular chains but also improve the adhesion of the composite hydrogel to the interface. These bio-based nanomaterials are inherently rigid, which is a prerequisite for the nanocomposite-based hydrogel enhancement strategy.[19] Yet, the realization of their full potential in improving the mechanical/adhesive properties of composite hydrogels requires the formation of strong interactions between the nanomaterials and the composite hydrogel molecular chains or between the interfaces.[20] This indicates that the surface structure of the nanomaterials, especially the content of surface polar groups, is crucial for improving the mechanical and adhesion properties of nanocomposite hydrogels.[21] Bio-based nanomaterials like CNC and CNF have a limited number of surface active hydroxyl groups, so the amount of carboxyl groups introduced on the CNC or CNF by TEMPO oxidation is low and has an upper limit (2–4 mmol g^{-1}), which restricts its scope of improving the performance of composite hydrogels.[22] Polymer grafting is a promising strategy that can further increase the content of polar groups on the surface of CNC or CNF by grafting molecules with carboxylated groups onto the surface, but it also has the problem of low grafting rate/grafting density.[23] Meanwhile, to the best of our knowledge, there are very few reports on the fabrication of bio-based nanomaterials with high surface carboxylation by increasing the grafting density. Therefore, it is still a challenge to prepare adhesive hydrogels with high mechanical, adhesive, conductive and long-lasting sensing properties.[7]

Herein, a strong, tough, and highly adhesive nanocomposite hydrogel (PACPH) is designed, and the mechanism based on surface-modified CNC with high carboxylation to improve the mechanical/adhesion properties is discussed. As shown in Fig. 1, PACPH was obtained by the *in situ* polymerization of AA/NaOH/SCNCPA/MBAA (*N*,*N*-methylene bisacrylamide) precursor under UV radiation. The special surface structure of SCNCPA led to the formation of abundant physical cross-links (strong chain entanglement and multiple hydrogen bonds) between SCNCPA and the new PAA molecular chains formed by *in situ* polymerization. Meanwhile, the rigid SCNCPA with abundant surface groups (–COOH, –OH, and $–OSO_3H$) enabled the formation of dense adhesion links between PACPH and different substrates since they act as anchor points, limiting the pull-out of the molecular chains at the interface. Due to the synergy of interfacial entanglement and densified adhesive groups, PAPCH obtained excellent mechanical and adhesion properties. While the tensile strength and fracture toughness increased from 0.34 to 1.45 MPa and 2.3 to 13.2 MJ m^{-3}, respectively, the adhesion strength increased by 2–3 times. By integrating the PACPH patch with electrodes, human electrocardiogram (ECG) signals in different states, such as resting and exercising states, could be monitored in real-time over a long period under stable conditions. Given the above advantages, it is reasonable to assume that PACPH and SCNCPA have a broad application prospect in the field of flexible sensors.

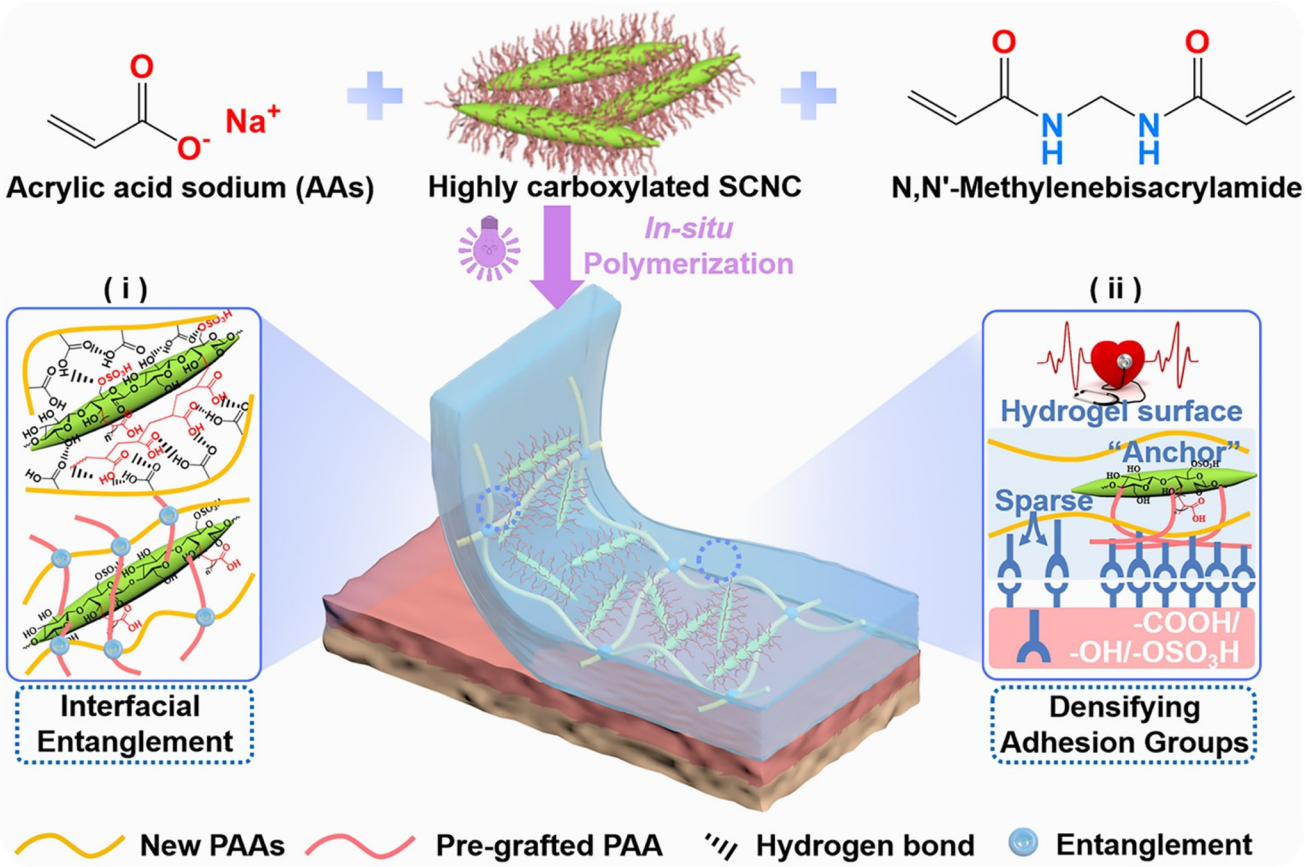

Fig. 1 A schematic illustration of the fabrication and network structure of the tough, highly adhesive/conductive nanocomposite hydrogel patch ($PACP_XH$; *X* is the content of SCNCPA).

Experimental details

Materials

Cotton pulp ($DP^{\frac{1}{n}}$ = 900) was supplied by Silver Hawk Co. Ltd (Gao mi, China). Sulfuric acid (H_2SO_4, 98 wt%), analytical-grade sodium hydroxide (NaOH), and methanol were purchased from Sinopharm Chemical Reagent Corporation (Shanghai, China). Acrylic acid was purchased from Tianjin Damao Chemical Reagent Co. Cerium ammonium nitrate (CAN), sodium citrate (SC), *N*,*N*′-methylene bisacrylamide (MBAA), and 2,2-diethoxyacetophenone were purchased from Aladdin Chemical Reagent Co. The water used in all experiments was deionized. All materials were used as received without further purification.

Preparation of SCNCPA by modifying cellulose nanocrystals to obtain a highly carboxylated surface

The preparation of the cellulose nanocrystals by the sulfate method (SCNC) is shown in Fig. S1.† The SCNC suspension was adjusted to pH = 7 and diluted to 0.5 wt%. A typical graft polymerization reaction involved the following steps. First, 20 mL of the 0.5 wt% SCNC suspension was added to a three-necked flask containing 0.9 mL of 0.1 mol L^{-1} SC solution, while O_2 in the three-necked flask was replaced with N_2 to provide an anaerobic environment for the polymerization reaction. Then, 0.04 g CAN was added as the initiator, followed by 0.6 mL of the AA monomer solution. Finally, the reaction was carried out at 35 °C for 2 h to obtain the reaction product. After the reaction, the reaction product was poured into a vacuum filtration device for extraction, during which deionized water was continuously passed to remove unreacted monomers and residual impurities. The product was then freeze-dried, ground into powder, and extracted with methanol at 80 °C for 24 hours to obtain a pure graft product without the homopolymer.

Preparation of $PACP_XH$ by the *in situ* polymerization of SCNCPA with the AA/NaOH precursor

Firstly, the SCNCPA powder was re-dispersed in water to obtain an aqueous dispersion of SCNCPA (solution A, 5 wt%, pH ≈ 7). Then, in order to minimize the discomfort that the carboxyl groups may cause to human skin, a sodium hydroxide (NaOH) solution was used to neutralize the acrylic monomer prior to polymerization so that the pH value of the precursor solution was close to neutral. The preparation steps of the AA/NaOH solution (solution B) with a monomer concentration of 40 wt%

and a degree of neutralization of 75% were as follows: 72 g of AA was added to a beaker containing 18 g of water and placed in a water bath at 25 °C with stirring; then, 90 g NaOH solution (33.3 wt%) was added to the beaker slowly (3 rpm) using a peristaltic pump under continuous stirring for 0.5 h to aid complete reaction. The purpose of slowly adding NaOH was to avoid its violent reaction with AA and the release of a large amount of heat, which would lead to the oxidation of AA in the air. Finally, the AA/NaOH/MBAA/SCNCPA solution with a monomer content of 30 wt% (solution C) was prepared as follows: A and B were mixed according to the added amount of SCNPA, stirred thoroughly, and then, a certain amount of MBAA (1.2 wt% of the monomer content) and 2,2-diethoxyacetophenone (0.6 wt% of the monomer content) were added and stirred thoroughly for 0.5 h. The PACP$_X$H nanocomposite hydrogels were obtained by pouring solution C into a dish with a plastic surface of a certain size (radius of 2 or 5 cm) and polymerizing it *in situ* for 30 min under UV light irradiation at a wavelength of 365 nm (X represents the amount of SCNCPA added).

Chemical structure characterization

The particle sizes of the dispersed particles in the AA/NaOH, AA/NaOH/SCNC, and AA/NaOH/SCNCPA solutions were tested by using dynamic light scattering (DLS). The FTIR spectra of freeze-dried PAAH, PACH, and PACPH were collected using a Bruker VERTEX 70 spectrometer and scanned 32 times in the reflection mode at 4000–400 cm^{-1} at a resolution of 4 cm^{-1}. The PAAH, PACH, and PACPH hydrogels were tested for Raman scattering using an incident light with a wavelength of 785 nm and resolution of 3 cm^{-1} using a Raman spectrometer (in *Via* Qontor, UK) in the presence of water. The XRD spectra of the PAAH, PACH and PACPH hydrogels were recorded after freeze-drying on a Rigaku Smart Lab diffractometer (Cu-Kα radiation, λ = 0.154 nm) at a scan rate of 5° min^{-1}. The crystallization information of the PAAH, PACH and PACPH hydrogels was further tested by two-dimensional small-angle X-ray scattering (SAXS, Xeuss 2.0 France). All samples were tested in the aqueous state under an incident X-ray Cu-Kα beam of λ = 1.5418 Å, and the distance from the sample to the detector was 2513 mm. The spectra were recorded using the two-dimensional detector Pilatus 300 K. The pixel size of Pilatus 300 K was 0.172 × 0.172 mm^2.

Microstructure characterization

The microscopic morphology of freeze-dried SCNC and SCNCPA powders, and PAAH, PACH and PACPH hydrogels was observed using a scanning electron microscope (JEOL SEM 6700) at an accelerating voltage of 10 kV. The transmission electron microscopic (TEM) images of SCNC and SCNCPA were acquired on a JEOL JEM-2100 FS instrument.

Mechanical properties

Solution C was poured into a dumbbell bar mould and gelatinized under UV irradiation to obtain the PACP$_X$H hydrogel, which was used to test the mechanical properties. The size information of the prepared dumbbell bar samples was as follows: all lengths were 40 mm, and the effective tensile length was 30 mm; all widths were 3.5 mm, and the thicknesses were measured using a thickness gauge prior to testing. Then, each sample was tested under the same program using a universal tensile machine (Instron 5943 Instron Instruments, USA). The testing procedure was as follows: prior to testing, the size information of the sample was entered into the computer software; the stress and strain information generated during the stretching process of the samples was collected using a 50 N force sensor. Three samples from each group were tested, and the median value was considered to remove the errors caused by defects and other extraneous conditions. Similarly, solution C was poured into a round-bottomed dish with a plastic surface to prepare samples under UV irradiation for testing the compression properties. Compression testing followed the same process as tensile testing, except for the differences in the fixtures used for the samples and the procedures used for the test.

Adhesion properties

The adhesion properties of the hydrogels were also tested on a universal testing machine. Firstly, samples of size 10 × 10 × 1.5 mm were prepared. Next, various matrix materials were prepared and cut into rectangular samples with a size of 60 × 20 mm. Then, the hydrogel was placed between the two base materials and some pressure was applied with fingers to ensure complete adhesion. Finally, the prepared sample was placed on the fixture of a universal testing machine and gradually pulled apart in the *Y*-direction (parallel to the contact surface between the hydrogel and the substrate) by stretching, and a 50 N force sensor was used to record the magnitude of the force due to the adhesion of the hydrogel to the substrate on both sides during the stretching process, as well as the displacement when it completely detached from the adhesion. Based on the information collected by the force transducer on the universal testing machine, the force *versus* displacement curves (*F*–*X*) were obtained for the adhesion failure process in the *Y*-direction for the PACPH hydrogel on different substrate surfaces. The maximum adhesion strength (in kPa) was calculated according to the maximum force value in the *F*–*X* curve and the contact area between the hydrogel and the substrate. The calculation formula is as follows:

$$\sigma = F/S$$

σ is the maximum adhesion strength (kPa), F is the maximum force value in the *F*–*X* curve (N), and S is the contact area between the PACPH hydrogel and the substrate (cm^2).

Conductivity and strain sensing

The electrical experiments were performed on an electrochemical workstation (CHI650E, CH Instruments, USA). The ionic conductivity of the different hydrogels was measured in the AC impedance mode. The sample size used for testing was 1 × 1 × 0.15 cm, and stainless steel iron sheets were used to clamp the sample on both sides to connect the electrodes. The

electrochemical workstation and small tensile tester (CMT-1503) were used to measure the current in the PACPH hydrogel sensor in real time under different strains and pressures and thus calculate the resistance change in the hydrogels under different states. The real-time monitoring of human motion by the PACPH hydrogel is achieved by connecting the two electrodes of the electrochemical workstation to the hydrogel using wires and adhering it to the human skin surface (*e.g.* fingers, wrists, laryngeal knots, knees, *etc.*).

ECG signal monitoring using the PACPH patch

The ACP precursor solution was poured into the groove containing the electrode for *in situ* polymerization under UV light to obtain the PACPH electrode patch. Then, the PACPH electrode patch was connected to the signal-receiving device through a wire and attached to the upper and lower sides of the left rib cage and the right rib cage of the human body and stabilized for a period of time. Finally, the changes in the ECG signals from the human body in different states, such as resting and exercising, were monitored in real-time along with the stability of the signals over a long period of time (by wearing the PACPH electrode patches for 1 h, 0.5 h and 24 h).

Results and discussion

Preparation and characterization of the PACP$_X$H hydrogel

The efficient grafting of CNC with the acrylic polymer was realized by our team[24,25] by using a synergistic initiation system of ceric ammonium nitrate (CAN) and sodium citrate (SC) (Fig. S1–S3†). Benefitted by the high grafting rate (205%), a large number of PAA molecular chains were grafted on the surface of sulfated CNC (SCNC), and the content of carboxyl groups on the surface was close to 11.5 mmol g^{-1}. Moreover, the grafted PAA (pH > p$K_{a\text{–}COOH}$) molecular chains were distributed on the surface of SCNC, and thus brush-like nanomaterials (SCNCPA) with gradient surfaces were obtained. Then, the PAAs/SCNCPA$_X$H nanocomposite hydrogels were prepared by the *in situ* radical polymerization of AA monomers, which was initiated by 2,2-diethoxyacetophenone under UV irradiation, in a homogeneous solution of AA/NaOH/SCNCPA/MBAA (ACPs, Fig. S4†), and named PACP$_X$H, with X denoting the content of SCNCPA (unless specified otherwise, X = 2). Fig. 1 demonstrates the detailed preparation process and the microstructure of PACPH, and Fig. 2A and C respectively show the physical images of PAAH and PACPH. The unique structure of SCNCPA (pre-grafted polyacrylic acid chains, $C_{\text{–}COOH} \approx$ 11.5 mmol g^{-1}) formed strong interfacial entanglement with the new PAA molecular chains, and on the other hand, it also densified the polar groups on the surface of PACPH, which worked in synergy to facilitate the simultaneous enhancement of both mechanical and adhesion properties of PACPH.

Fig. S5A† illustrates the uniform dispersion of both SCNC and SCNCPA at the nanoscale in the AA/NaOH precursor solution (clear Tyndall effect), and the stability of the dispersion was also illustrated by the zeta potential (Fig. S5D†). After the addition of SCNCPA, PACPH appeared as a milky white material with a slight bluish tint and maintained a certain degree of transparency (Fig. 2C). This will expand the application scope of PACPH, such as the observation of interface

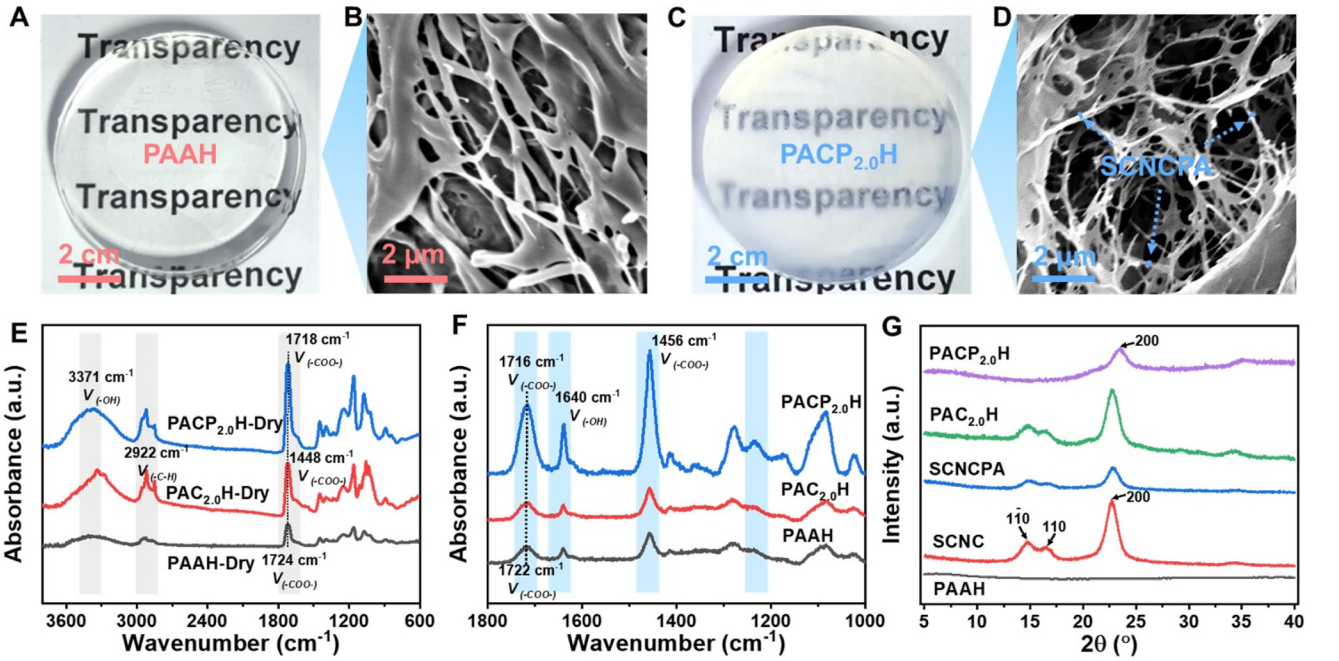

Fig. 2 (A and C) The optical images of PAAH and PACPH. (B and D) The SEM images of PAAH and PACPH after freeze-drying. (E) The FTIR spectra of PAAH, PACH and PACPH after freeze-drying. (F) The Raman spectra of the three hydrogels in the aqueous state (considering the effect of water on hydrogen bonding). (G) The XRD spectra of SCNC and SCNCPA powders and the three hydrogels after freeze-drying.

changes in real-time. Due to the addition of SCNCPA, the nanoparticles dispersed in the ACP homogeneous solution existed in two sizes, of which the size close to 110 nm can be attributed to SCNCPA (Fig. S5B and C†). From the TEM images of SCNCPA (Fig. S2D–F†), it could be seen that after grafting PAA, its surface was coated by the polymer, resulting in a rougher surface and larger particle size (the diameter increased from 20 to 50 nm compared with SCNC), which was also confirmed by the SEM images of SCNCPA (Fig. S3†). Interestingly, the SEM images showed that both SCNC and SCNCPA tended to self-assemble to form nanofibers after freeze-drying due to compression by ice crystals, which is very favorable for energy dissipation in their composite hydrogels.[26]

Fig. 2B and D display the SEM images of PAAH and PACPH after freeze-drying. Because the AA monomer was partially neutralized by NaOH prior to use, a large amount of Na^+ was present in both PAAH and PACPH, leading to difficulties in achieving complete freeze-drying and the formation of an irregular pore structure (Fig. S6†). In the microstructure of PACPH (Fig. 2D), most of the self-assembled SCNCPA nanofibers were interconnected with or buried in the PAA matrix. Combined with the structure of SCNCPA, we speculated that the reason for the formation of this microstructure during the *in situ* polymerization process is that the PAA molecular chains distributed on the surface of SCNCPA interpenetrate with the new PAAs formed during the polymerization process (Fig. S4B†), resulting in the formation of strong entangled chains between SCNCPA and the new formed PAA molecular chains.

In order to verify the multiple hydrogen bonds between SCNCPA and the new PAA molecular chains, PACPH was characterized in both dry and aqueous states using FTIR and Raman spectroscopy. As shown in Fig. 2E, fully freeze-dried PAAH showed two broad peaks centered at 3371 and 2922 cm^{-1}, which could be attributed to the stretching vibrations of –OH and $–CH_2$, and two sharp peaks at 1724 and 1450 cm^{-1}, which belonged to the two stretching vibrations (symmetric and asymmetric) of $–COO^-$. However, the addition of SCNCPA resulted in the redshift of the absorption peak of $–COO^-$ in PACPH (from 1724 to 1716 cm^{-1}), while its intensity was significantly increased, which indicates that the overall strength and density of hydrogen bonds in PACPH had improved due to the formation of multiple hydrogen bonds between SCNCPA and the PAA molecular chain networks.[27] The presence of multiple hydrogen bond interactions was further confirmed by comparing the Raman spectra of PAAH and PACPH (Fig. 2F).[28] Although SCNCPA was covered with a layer of amorphous PAA molecular chains, the grafting reaction did not affect its crystal structure (the crystal shape was unchanged, Fig. 2G).[29] Therefore, the presence of crystal structure in PACPH and the absence of crystal structure in PAAH, as shown by the X-ray diffraction pattern (Fig. 2G) and the small-angle X-ray diffraction spectrum (SAXS, Fig. S7†), are also reasons for the differences in their mechanical properties.[30] In addition, the SXRS spectra of PACPH also showed that SCNCPA was uniformly dispersed in PACPH.

In the above discussion, the changes in the chemical structure and microstructure of PACPH after the addition of SCNCPA nanomaterials are explained. SCNCPA with a highly carboxylated surface ($C_{–COOH} \approx 11.5$ mmol g^{-1}) and gradient structure (surface pre-grafted molecular chains) was obtained by the surface grafting modification of SCNC (Fig. S1–S3†). The special structure of SCNCPA allows the formation of dense hydrogen bonds and strong chain entanglement between SCNCPA and the hydrogel molecular chain network in PACPH. When subjected to external forces, these forces are transmitted to SCNCPA *via* the molecular chains and chain entanglements and result in the displacement of SCNCPA, dissipating a large amount of energy. Meanwhile, these hydrogen bonds and chain entanglements dissociate with the displacement of SCNCPA, which further increases energy dissipation and thus improves the mechanical properties of PACPH.[13]

Mechanical properties and fatigue resistance of the $PACP_XH$ hydrogels

The mechanical properties of the PAAH, PAC_XH (composite unmodified CNC), and $PACP_XH$ hydrogels were evaluated by uniaxial tensile tests at room temperature, and the results are shown in Fig. 3A, B, D, and E. PAAH has poor mechanical properties (low modulus (22 kPa)/strength (0.34 MPa)/fracture toughness (2.3 MJ m^{-3}) and high deformation (1680%)) and is a typical soft and weak material.[18] This is due to the single and sparse internal network structure of PAAH, which lacks suitable energy dissipation mechanisms. The strength and modulus of PAC_XH had increased significantly (in the small strain, elastic region) after the addition of SCNC (Fig. 3D). This is attributed to the fact that PACH can transfer the force to SCNC when subjected to external forces and cause SCNC to migrate, which dissipates a large amount of energy and thus improves the mechanical properties. $PACP_XH$ had higher strength and modulus under the same conditions (Fig. 3D and E). In addition, the strength and modulus of $PACP_XH$ were directly proportional to the content of SCNCPA, and the toughness increased initially and then decreased with increasing content (Fig. 3B). When the SCNCPA content was X = 2 wt%, the overall mechanical properties of $PACP_XH$ were optimal, with strength, modulus, and toughness reaching 1.45 MPa, 332 kPa, and 13.2 MJ m^{-3}, respectively (Fig. 3B and E). Fig. 3C shows that PACPH can be stretched up to 20 times its own length (Fig. 3C) without fracture and can also lift weights up to 200 g (Fig. 3F, ≈ 500 times its own weight).

A small number of permanent chemical cross-linking points (MBAA) exist within PACPH. The loading-unloading experiments also showed that PACPH has good elasticity and fatigue resistance (Fig. 3G and H), and the shape recovery rate was 92 ± 2% after 1000 cycles (Fig. 3I).[31] In addition, a hysteresis regression line appeared on the loading-unloading curve of PACPH, suggesting the existence of certain non-covalent interactions within PACPH. To further verify the existence of noncovalent interactions within PACPH, we analyzed the rheological properties of SCNCPA suspensions and the three hydrogels. As seen in Fig. S8E–G,† the SCNCPA suspensions showed

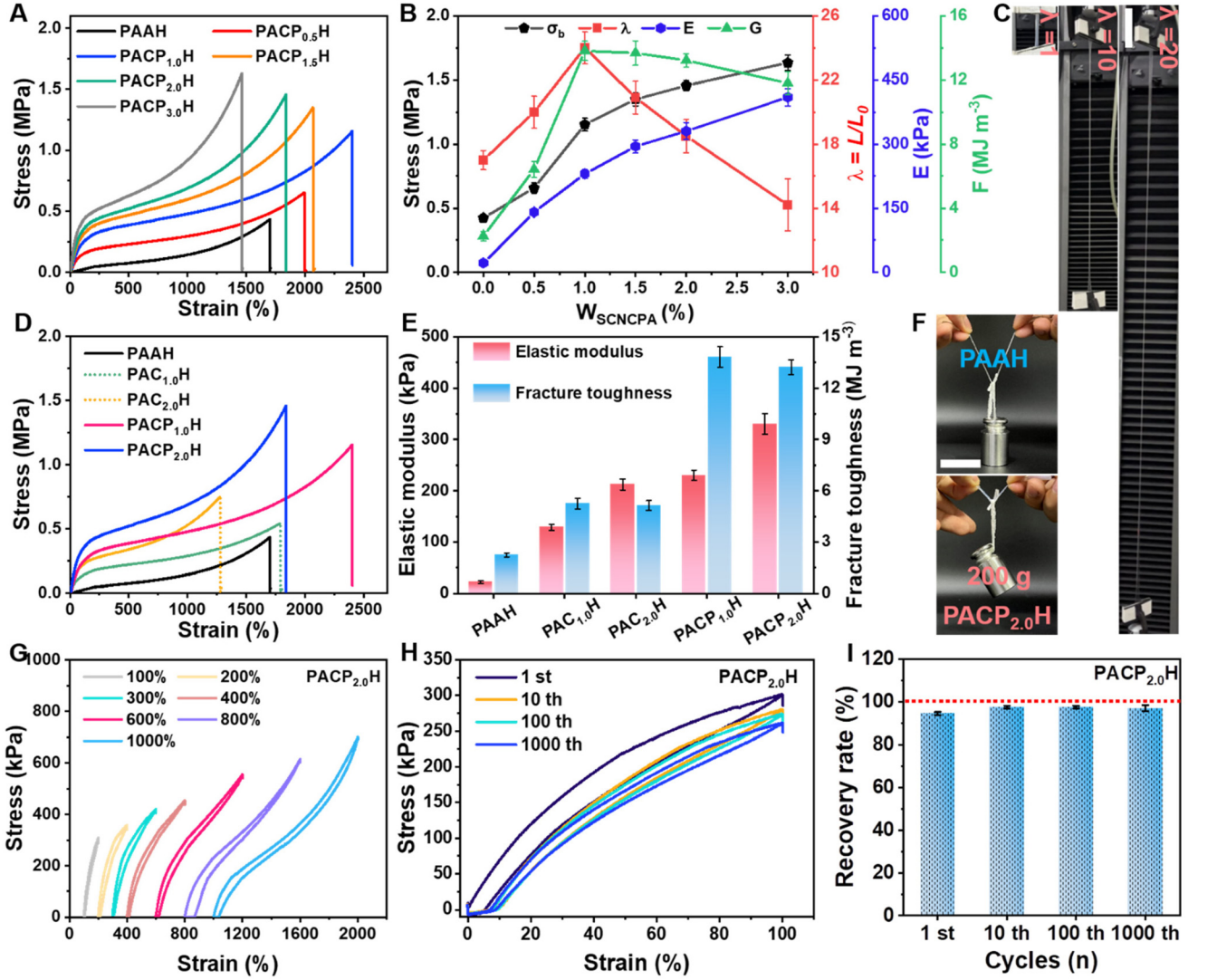

Fig. 3 (A) Tensile stress–strain curves of PAAH and PACP$_X$H. (B) Trends of tensile strength, strain, elastic modulus, and fracture toughness of PACP$_X$H with an increasing SCNCPA content. (C) The photographs of the PACPH hydrogel at different tensile ratios. (D and E) The tensile stress–strain curves, elastic modulus and fracture toughness of PAAH, PAC$_X$H, and PACP$_X$H. (F) Demonstration of PAAH and PACPH lifting weights. (G) Tensile loading–unloading curves of PACPH when stretched to achieve different strains. (H and I) Stress–strain curves and deformation recovery rates of PACPH hydrogels after different numbers of stretching cycles.

a clear viscoelastic transition from viscous fluids ($G' < G''$) to elastic solids ($G' > G''$) at concentrations above 2.4 wt%. This phenomenon was not observed in the unmodified SCNC suspension. This suggests that strong interactions between SCNCPA molecules are formed due to the intertwining of the molecular chains of the surface grafts, resulting in a three-dimensional network structure when the concentration exceeds a critical level. The rheological properties of the three hydrogels further verified this observation. Under the same conditions, PACPH had higher G' and G'', which remained stable at a wide range of frequencies, which proves the existence of non-covalent interactions, such as hydrogen bonds and chain entanglement, within PACPH. Meanwhile, this also explains why PACP$_{2.0}$H has the best overall mechanical properties, *i.e.*, the SCNCPA concentration reaches a critical level to form a percolation network structure, which interpenetrates and entangles with the hydrogel network, increasing the energy dissipation caused by SCNCPA displacement.

Then, the compressive properties of the composite hydrogels were evaluated, and the results are shown in Fig. S8A–F.† The addition of SCNCPA improved the compressive strength of the composite hydrogels. However, due to the presence of numerous noncovalent interactions, there was a certain hysteresis in the shape recovery of PACPH after compression (Fig. S8A–C†). Overall, as shown in Fig. 4A, the composite hydrogel PACPH had excellent integrated mechanical properties, which originate from effective energy dissipation by the rigid SCNCPA along with the pre-grafted molecular chains on the surface due to the synergistic effect of self-displacement and dissociation of the non-covalent interactions during the

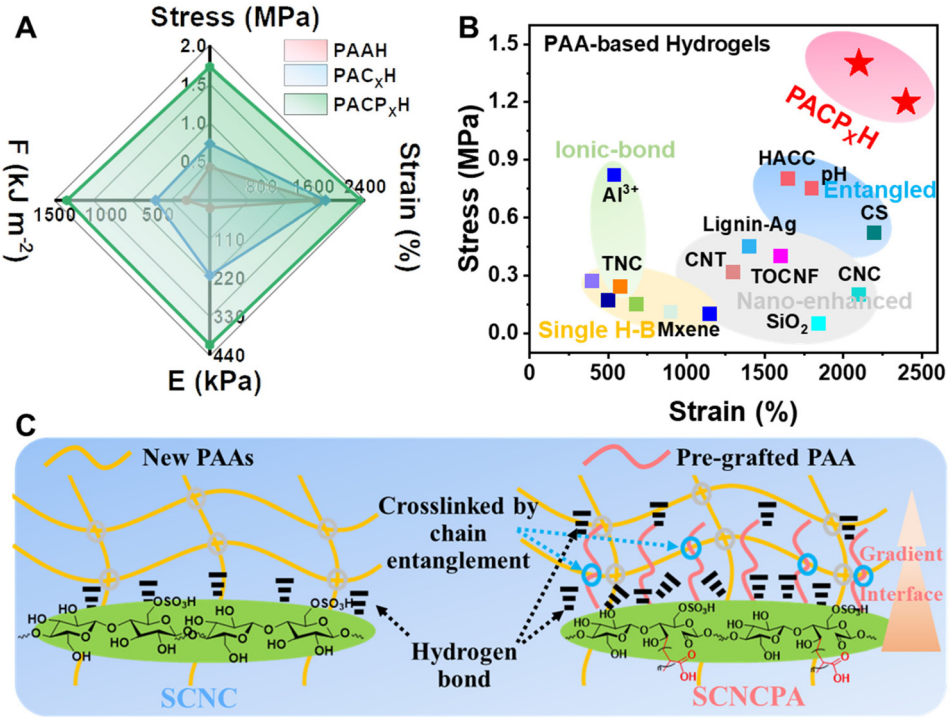

Fig. 4 (A) The radar plot of the comprehensive mechanical properties of PACPH. (B) Comparison of the maximum tensile strength and strain at break of PACPH with the currently used PAA-based hydrogels. (C) Strengthening and toughening mechanism of SCNCPA with abundant carboxylate groups on the surface and the gradient structure (pre-grafted molecular chains) in a single hydrogel network.

deformation process. Under the same conditions, the composite hydrogel PACPH prepared from SCNCPA exhibited higher strength and larger deformation (Fig. 4B),[9,11,12,18–21,32–40] which are favorable to the application of hydrogels in environments requiring high strength. Finally, based on the above analysis and the surface structure of SCNCPA, its mechanism towards the enhancement and toughening of the hydrogel is shown in Fig. 4C. More and stronger non-covalent interactions (hydrogen bonds and chain entanglements) are formed between SCNCPA with a gradient surface structure (abundant polar groups, pre-grafted molecular chains) and the molecular chains of the hydrogel. When subjected to an external force, the displacement of SCNCPA and the dissociation of these interactions work together to dissipate a large amount of energy during the deformation of the composite hydrogel, resulting in excellent mechanical properties.

Adhesion properties of the PACPH hydrogels and discussion on the adhesion-densifying mechanisms

Considering that hydrogel-based flexible sensors need to maintain stable and strong adhesion with various substrate materials in practical applications, the adhesion performance of PACPH on different substrate materials was investigated. Fig. 5A shows the schematic of the hydrogel adhesion test: the PACPH patch (1.0 × 1.0 × 0.15 cm^3) was fully adhered to the substrate on both sides and then stretched along the *Y*-axis direction; the forces and displacements (*F*–*X*) generated in the process of de-adhesion were recorded. From the *F*–*X* curves (Fig. 5B), it can be seen that the PACPH patch has good adhesion performance on different substrates, and its maximum adhesion force reached 5.5 N cm^{-1}. The maximum adhesive strength of PACPH to different substrates was calculated using the formula $\sigma = F/S$.[41] The results show that the maximum adhesive strength to different substrates ranged from 32–65 kPa (Fig. 5C). The adhesion performance of the PACPH patch on fingers and different substrates (including but not limited to human skin, glass, rubber, plastic, metal, fruit peel and wood) is demonstrated in Fig. 5D; the maximum weight it could lift was 245 g, which clearly illustrates the nice interfacial adhesion performance of the PACPH patch. In addition, using the glass substrate as the reference, the adhesion performance of PACPH is better than most of the currently used PAA-based hydrogels (Fig. 5E).[9,18,20,32,37,38,40–48]

In order to reveal the mechanism of SCNCPA toward improving the adhesion performance of composite hydrogels, we systematically compared the adhesion properties of PAAH, PACH, PACPH, and PACP$_X$H with different SCNCPA contents using the glass substrate as reference. First, as seen in Fig. 5F and G, PAAH had the lowest adhesion performance with an adhesion strength of only 15 ± 0.5 kPa and was prone to debonding; PACH demonstrated moderate adhesion, and PACPH possessed the highest adhesion force and adhesion strength (5.5 N cm^{-1} and 44 ± 2 kPa). This suggests that the unique structure of SCNCPA could densify the connection between the PACPH-substrate interfaces. Fig. S9B and C† show that the adhesion performance of PACP$_X$H increased with the increase

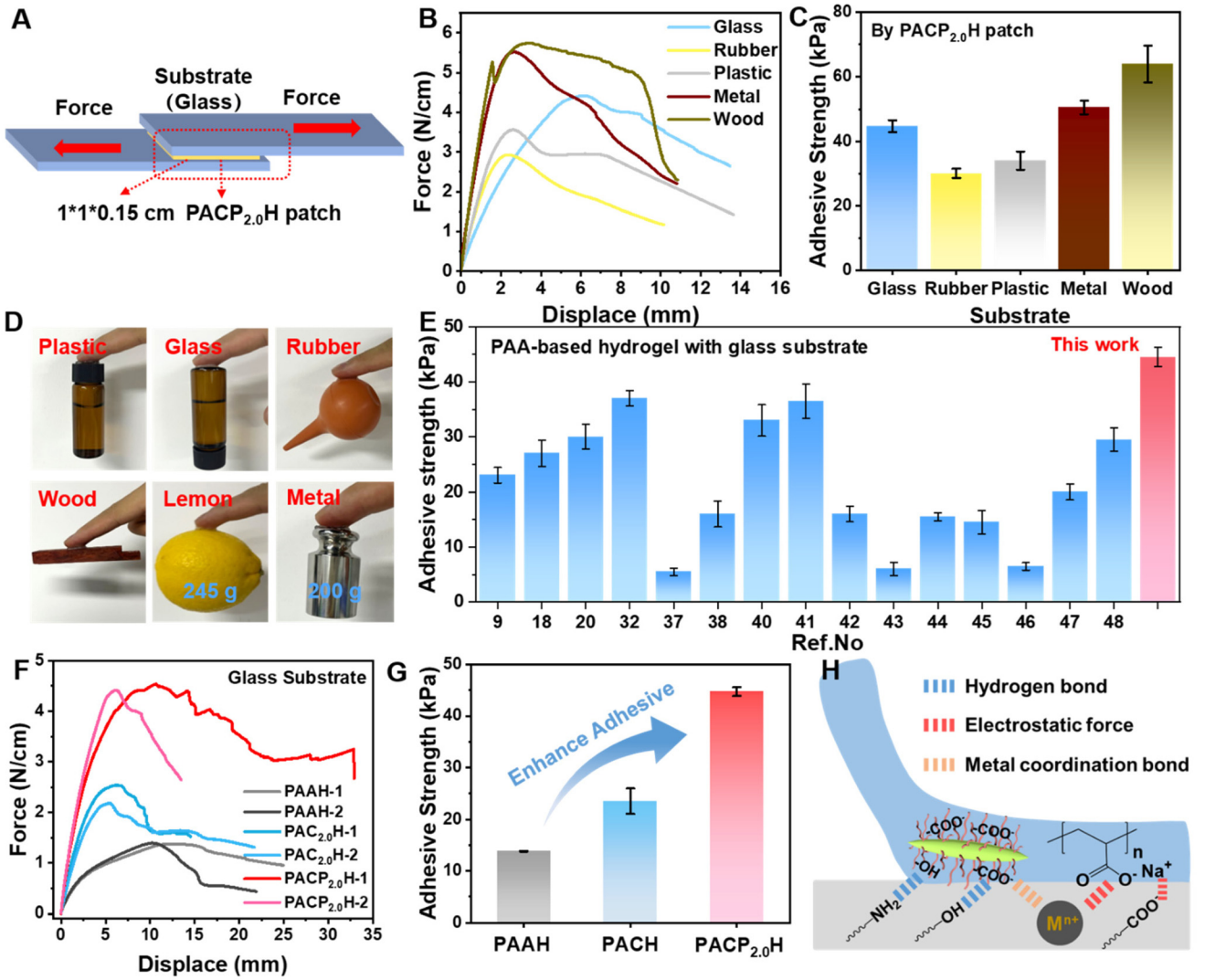

Fig. 5 (A) A schematic of the hydrogel patch adhesion performance test. (B, C and D) The force-displacement (F–X) curves, maximum adhesion strength and photographic representations (including maximum adhesion lifting weights, m = 245 g, 200–300 times its weight) of the PACPH hydrogel on different substrates. (E) Comparison of the maximum adhesion strength of the PACPH hydrogel with the currently used PAA-based adhesive hydrogels. (F and G) The F–X curves and maximum adhesion strengths of PAAH, PACH and PACPH on the glass substrate. (H) The mechanism of SCNCPA toward improving the interfacial adhesion of the PACPH hydrogels to various substrates.

in X, further verifying the role of SCNCPA in improving adhesion performance. A large amount of water was present in PAAH (≈65 wt%, Fig. S10A†) and filled in the network of PAA molecular chains, which lowered the content and density of polar groups on the surface of the PAAH hydrogel.[49] Meanwhile, the greater mobility of the molecular chains is unfavourable for the establishment of effective adhesion linkages with different substrates (fewer linkages, and immobilized molecular chains). In addition, the poor mechanical properties of PAAH also lower the resistance to damage at the bonding interface (easily deformed and damaged). Therefore, the mechanism of SCNCPA toward improving the adhesion performance of PACPH is shown in Fig. 5H. First, the abundant polar groups (–OH/–COOH, *etc.*) on the surface of SCNCPA increase the density of polar groups on the surface of PACPH, leading to the formation of more non-covalent interactions (hydrogen bonds, electrostatic attraction, metal coordination, *etc.*) with the surface groups of different substrates. The dissociation of these interactions during the debonding process contributes to the improvement of the interfacial adhesion energy. Secondly, the components of adhesion energy include cohesion energy and interfacial adhesion energy.[50] The rigid SCNCPA enhances the mechanical properties of PACPH, which results in the higher cohesion energy of PACPH, thereby increasing the energy dissipated during deformation due to debonding. These two aspects act synergistically towards improving the adhesion properties of PACPH.

Potential applications of the PACPH patch in wearable sensors and long-lasting cardiac electrode patches

During the preparation process (Fig. S4†), a large amount of Na^+ is introduced, resulting in the good ionic conductivity of PAAH and PACPH (Fig. S10C and D†). Using the ionic conductivity equation $\rho = L/RS$ (L is the thickness of the sample, R is the impedance value of the sample, and S is the contact area between the sample and the electrolytic sheet), the conductivity of PACPH was calculated to be approximately 4.16 S m^{-1}, which illustrates its good ionic conductivity.[51] The ionic conductivity of PACPH was slightly higher than that of PAAH (3.41 S m^{-1}) mainly due to the fact that a certain amount of Na^+ was also present in the SCNCPA dispersion, increasing the ionic concentration inside the composite hydrogel. The currents of the three hydrogels remained nearly stable at a constant voltage, illustrating their stable conductivity (Fig. S11A†). In addition, during stretching or compressive deformation, restricted by changes in the network structure, the electrical conductivity of PACPH responded accordingly. For example,

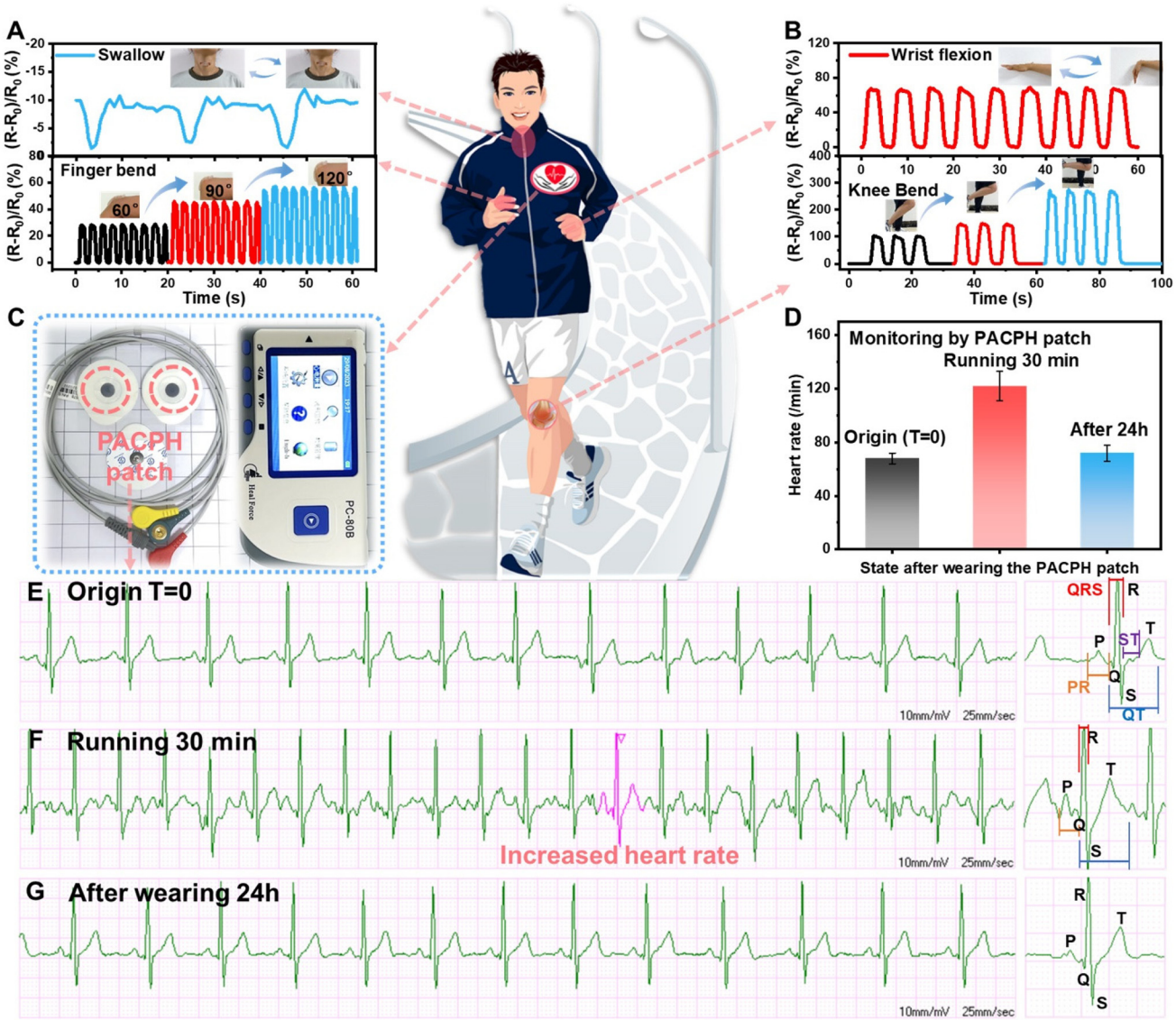

Fig. 6 Potential applications of the PACPH patch. Metal electrodes were attached to both sides of the PACPH hydrogel and connected to the electrochemical workstation; then, the PACPH patch was attached to different locations in the human body to monitor human activity based on the changes in current caused by changes in the activity, such as (A) swallowing (top) and bending of the fingers (bottom) and (B) bending of the wrists (top) and bending of the knees when walking (bottom). (C) The photographic image of a long-lasting ECG-electrode-integrated PACPH patch and the device used to monitor the ECG signal. The red circles denote the PACPH patch that is responsible for stable adhesion to the human skin and conductive sensing. (D) The variation in human heart rate during different activity states during long-term monitoring lasting one day using the PACPH ECG electrode patches. The real-time electrocardiograms of humans monitored using PACPH ECG electrode patches under different activity states: (E) initial state, (F) after 30 min of exercise, and (G) after 24 h; the enlarged images are provided on the right.

cyclic stretching with different stretching ratios (Fig. S11B†) resulted in a stepwise change in the current of PACPH under constant conditions. When PACPH was continuously stretched to 1600% deformation, the relative resistance changed, as shown in Fig. S11D,† resulting in different sensing factors (GF, defined as $(R - R_0)/R_0$) in different deformation ranges. Fig. S11D† also indicates that PACPH has good sensing capability over a wide range of strains. For example, in the 100-cycle test at 400% strain, PACPH demonstrated stable sensing performance, as well as a fast response (Fig. S12A,† response time ≈ 1 s). At low strains, PACPH demonstrated even more stable sensing capabilities (Fig. S12B,† 100% strain, 1000 cycles of stabilization). At the same time, PACPH also showed responsiveness to compression stimulation (Fig. S11C and E†).

Given the appealing mechanical, adhesion, electrical conductivity and sensing properties of the PACPH patches, we tested their potential application in wearable sensing, as well as for monitoring the daily activities of humans. The PACPH patch was connected to an electrochemical workstation *via* metal electrodes and wires, and then attached to different locations in the human body, such as throat/fingers (Fig. 6A) and wrist/knees (Fig. 6B), to monitor various human activities in real-time, such as drinking water, writing, playing ball and walking. We found that using the PACPH patch in conjunction with metal button electrodes has great potential for application in monitoring human electrocardiogram (ECG) signals as well. Fig. 6C shows the schematic of the long-lasting ECG electrode patch prepared based on the PACPH patch, and the signal receiving and processing device. By attaching the PACPH-based ECG electrode patch, as indicated in Fig. S13,† to the skin surface of the human body, real-time ECG signals could be obtained (Fig. 6D, Fig. S14†). For example, the heart rate was stable in the resting state (68 ± 4 min^{-1}) and accelerated in the exercising state (122 ± 11 min^{-1}). Further, the ECG signal became disordered, as indicated by the increase in P-wave amplitude, shortening of the time of the QRS segment, and elevation of the ST segment and other changes (Fig. 6D–F). In addition, benefiting from the strong and stable adhesion of PACPH, the PACPH-based ECG electrode patches could be used to monitor ECG signal changes stably for a long period of time under different exercise states (Fig. 6G, Fig. S14†). The device delivered stable monitoring even when attached to the surface of the human body for 24 hours. Visualization of the ECG signals obtained using the PACPH ECG electrode patch during exercise has a high significance in human health management as this can effectively avoid potential hazards (heart rate irregularity or coronary artery pathology) while exercising or cardiac hazards due to over-exercising.

Conclusions

In summary, we have developed a tough, highly adhesive and conductive nanocomposite hydrogel (PACPH) *via* the synergy of strong interfacial entanglement and adhesion group densification. PACPH was obtained by the *in situ* polymerization of highly carboxylated cellulose nanocrystals (SCNCPA) and acrylic acid sodium precursors. SCNCPA, which was obtained by efficient grafting of SCNC with PAA, showed a gradient structure (pre-grafted molecular chain) with abundant polar groups (≈12.0 mmol g^{-1}, –OH, –COOH, –OSO_3H). This special structure enhanced the interfacial entanglement between SCNCPA and the hydrogel network in PACPH. When subjected to external forces, the displacement of SCNCPA and the dissociation of interfacial entanglement aided in dissipating a significant amount of energy, thus improving the mechanical properties of PACPH. The tensile strength, modulus, and fracture toughness of PACPH reached 1.45 MPa, 332 kPa, and 13.2 MJ m^{-3}, respectively. In addition, the abundant polar groups on the surface of SCNCPA solved the problem of sparse polar groups on the surface of the hydrogel. Therefore, densifying the adhesive groups and high energy dissipation synergistically improved the adhesion properties of PACPH, which demonstrated an adhesion force of 5.5 N cm^{-1} and an adhesion strength of 65 kPa. The excellent and stable electrical conductivity of PACPH further endows it with more application potentials, such as long-lasting and stable monitoring of human activities and ECG signals under different exercise states, which is essential to promoting adhesive hydrogels in human health management.

Author contributions

Yunjie Lu: Conceptualization, methodology, writing original draft. Zhaohui Li: Investigation, data curation. Zewei Li: Methodology. Shihao Zhou: Investigation. Ning Zhang: Resources. Jianming Zhang: Supervision, writing-reviewing. Lu Zong: Supervision, writing-reviewing and editing.

Conflicts of interest

The authors declare no conflicts of interest.

Acknowledgements

National Natural Science Foundation of China (No. 51903134) and State Key Laboratory of Organic–Inorganic Composites (oic-202201009) are kindly acknowledged for financial support.

References

1 L. Hu, P. L. Chee, S. Sugiarto, Y. Yu, C. Shi, R. Yan, Z. Yao, X. Shi, J. Zhi, D. Kai, H. D. Yu and W. Huang, *Adv. Mater.*, 2023, **35**, 2205326.
2 Z. Wang, H. Wei, Y. Huang, Y. Wei and J. Chen, *Chem. Soc. Rev.*, 2023, **52**, 2992–3034.
3 X. Liu, J. Liu, S. Lin and X. Zhao, *Mater. Today*, 2020, **36**, 102–124.
4 J. Yang, R. Bai, B. Chen and Z. Suo, *Adv. Funct. Mater.*, 2019, **30**, 1901693.

5 Y. Zhao, S. Song, X. Ren, J. Zhang, Q. Lin and Y. Zhao, *Chem. Rev.*, 2022, **122**, 5604–5640.
6 Y. S. Zhang and A. Khademhosseini, *Science*, 2017, **356**, eaaf3627, DOI: **10.1126/science.aaf3627**.
7 H. Zhao, M. Liu, Y. Zhang, J. Yin and R. Pei, *Nanoscale*, 2020, **12**, 14976–14995.
8 Z. Qin, G. Zhao, Y. Zhang, Z. Gu, Y. Tang, J. T. Aladejana, J. Ren, Y. Jiang, Z. Guo, X. Peng, X. Zhang, B. B. Xu and T. Chen, *Small*, 2023, 2303038, DOI: **10.1002/smll.202303038**.
9 K. Shen, Z. Liu, R. Xie, Y. Zhang, Y. Yang, X. Zhao, Y. Zhang, A. Yang and Y. Cheng, *Mater. Horiz.*, 2023, **10**, 2096–2108.
10 Y. Wang, Q. Chang, R. Zhan, K. Xu, Y. Wang, X. Zhang, B. Li, G. Luo, M. Xing and W. Zhong, *J. Mater. Chem. A*, 2019, **7**, 24814–24829.
11 L. Han, K. Liu, M. Wang, K. Wang, L. Fang, H. Chen, J. Zhou and X. Lu, *Adv. Funct. Mater.*, 2018, **28**, 1704195.
12 X. Li, L. He, Y. Li, M. Chao, M. Li, P. Wan and L. Zhang, *ACS Nano*, 2021, **15**, 7765–7773.
13 D. Hu, M. Zeng, Y. Sun, J. Yuan and Y. Wei, *SusMat*, 2021, **1**, 266–284.
14 D. Zhao, B. Pang, Y. Zhu, W. Cheng, K. Cao, D. Ye, C. Si, G. Xu, C. Chen and H. Yu, *Adv. Mater.*, 2022, **34**, e2107857.
15 F. Lin, Z. Wang, Y. Shen, L. Tang, P. Zhang, Y. Wang, Y. Chen, B. Huang and B. Lu, *J. Mater. Chem. A*, 2019, **7**, 26442–26455.
16 Y. Ko, G. Kwon, H. Choi, K. Lee, Y. Jeon, S. Lee, J. Kim and J. You, *Adv. Funct. Mater.*, 2023, **33**, 2302785.
17 Y. Qin, J. Mo, Y. Liu, S. Zhang, J. Wang, Q. Fu, S. Wang and S. Nie, *Adv. Funct. Mater.*, 2022, **32**, 2201846.
18 X. Yao, S. Zhang, L. Qian, N. Wei, V. Nica, S. Coseri and F. Han, *Adv. Funct. Mater.*, 2022, **32**, 2204565.
19 T. Zhang, Q. Cheng, D. Ye and C. Chang, *Carbohydr. Polym.*, 2017, **169**, 139–148.
20 H. Zhou, J. Lai, B. Zheng, X. Jin, G. Zhao, H. Liu, W. Chen, A. Ma, X. Li and Y. Wu, *Adv. Funct. Mater.*, 2021, **32**, 2108423.
21 X. Fan, Y. Fang, W. Zhou, L. Yan, Y. Xu, H. Zhu and H. Liu, *Mater. Horiz.*, 2021, **8**, 997–1007.
22 M. Cheng, Z. Y. Qin, Y. Y. Chen, J. M. Liu and Z. C. Ren, *Cellulose*, 2017, **24**, 3243–3254.
23 S. Wohlhauser, G. Delepierre, M. Labet, G. Morandi, W. Thielemans, C. Weder and J. O. Zoppe, *Macromolecules*, 2018, **51**, 6157–6189.
24 Y. Liu, H. Xu, L. Zhou and J. Zhang, *Green Chem.*, 2023, **25**, 3027–3033.
25 Y. X. Liu, Y. J. Lu, H. Zhang, X. R. Liu, Z. Q. Kong, L. J. Zhou, H. Liu and J. M. Zhang, *Green Chem.*, 2021, **23**, 8581–8590.
26 N. Peng, D. Huang, C. Gong, Y. Wang, J. Zhou and C. Chang, *ACS Nano*, 2020, **14**, 16169–16179.
27 W. Zhang, B. Wu, S. Sun and P. Wu, *Nat. Commun.*, 2021, **12**, 4082.
28 Y. Wy, J. Park, S. Huh, H. Kwon, B. S. Goo, J. Y. Jung and S. W. Han, *Nanoscale*, 2023, **15**, 1537–1541.
29 L. Zhou, N. Li, J. Shu, Y. Liu, K. Wang, X. Cui, Y. Yuan, B. Ding, Y. Geng, Z. Wang, Y. Duan and J. Zhang, *ACS Sustainable Chem. Eng.*, 2018, **6**, 12403–12410.
30 N. Zhang, B. Zhang, Y. Pang, H.-S. Yang, L. Zong, Y.-X. Duan and J.-M. Zhang, *Chin. J. Polym. Sci.*, 2022, **40**, 373–383.
31 S. Lin, X. Liu, J. Liu, H. Yuk, H. C. Loh, G. A. Parada, C. Settens, J. Song, A. Masic, G. H. McKinley and X. Zhao, *Sci. Adv.*, 2019, **5**, eaau8528.
32 S. Afewerki, X. Wang, G. U. Ruiz-Esparza, C.-W. Tai, X. Kong, S. Zhou, K. Welch, P. Huang, R. Bengtsson, C. Xu and M. Strømme, *ACS Nano*, 2020, **14**, 17004–17017.
33 B. Li, Y. Zhang, C. Wu, B. Guo and Z. Luo, *Carbohydr. Polym.*, 2018, **198**, 1–8.
34 S.-N. Li, Z.-R. Yu, B.-F. Guo, K.-Y. Guo, Y. Li, L.-X. Gong, L. Zhao, J. Bae and L.-C. Tang, *Nano Energy*, 2021, **90**, 106502.
35 B. Liu, F. Li, P. Niu and H. Li, *ACS Appl. Mater. Interfaces*, 2021, **13**, 21822–21830.
36 Y. Liu, Y. Lei, L. Hua, J. Lu, K. Wang and C. Zhao, *Chem. Mater.*, 2021, **33**, 8351–8359.
37 W. Ma, W. Cao, T. Lu, Z. Jiang, R. Xiong, S. K. Samal and C. Huang, *ACS Appl. Mater. Interfaces*, 2021, **13**, 58048–58058.
38 T. Wang, X. Ren, Y. Bai, L. Liu and G. Wu, *Carbohydr. Polym.*, 2021, **254**, 117298.
39 X. Q. Wang, K. H. Chan, W. Lu, T. Ding, S. W. L. Ng, Y. Cheng, T. Li, M. Hong, B. C. K. Tee and G. W. Ho, *Nat. Commun.*, 2022, **13**, 3369.
40 X. Yu, Y. Zheng, H. Zhang, Y. Wang, X. Fan and T. Liu, *Chem. Mater.*, 2021, **33**, 6146–6157.
41 G. Huang, Z. Tang, S. Peng, P. Zhang, T. Sun, W. Wei, L. Zeng, H. Guo, H. Guo and G. Meng, *Macromolecules*, 2021, **55**, 156–165.
42 H. Bai, Z. Zhang, Y. Huo, Y. Shen, M. Qin and W. Feng, *J. Mater. Sci. Technol.*, 2022, **98**, 169–176.
43 X. He, Z. Li, J. Li, D. Mishra, Y. Ren, I. Gates, J. Hu and Q. Lu, *Small*, 2021, **17**, 2103521.
44 Y. Liang, K. Wang, J. Li, H. Wang, X. Q. Xie, Y. Cui, Y. Zhang, M. Wang and C. S. Liu, *Adv. Funct. Mater.*, 2021, **31**, 2104963.
45 Q. Ling, W. Liu, J. Liu, L. Zhao, Z. Ren and H. Gu, *ACS Appl. Mater. Interfaces*, 2022, **14**, 24741–24754.
46 C. Shao, M. Wang, L. Meng, H. Chang, B. Wang, F. Xu, J. Yang and P. Wan, *Chem. Mater.*, 2018, **30**, 3110–3121.
47 X. Su, Y. Luo, Z. Tian, Z. Yuan, Y. Han, R. Dong, L. Xu, Y. Feng, X. Liu and J. Huang, *Mater. Horiz.*, 2020, **7**, 2651–2661.
48 H. Zhou, J. Lai, X. Jin, H. Liu, X. Li, W. Chen, A. Ma and X. Zhou, *Chem. Eng. J.*, 2021, **413**, 127544.
49 N. Cohen, C. Du and Z. L. Wu, *Macromolecules*, 2021, **54**, 11316–11325.
50 Z. Pan, Q. Q. Fu, M. H. Wang, H. L. Gao, L. Dong, P. Zhou, D. D. Cheng, Y. Chen, D. H. Zou, J. C. He, X. Feng and S. H. Yu, *Nat. Commun.*, 2023, **14**, 5378.
51 C. C. Kim, H. H. Lee, K. H. Oh and J. Y. Sun, *Science*, 2016, **353**, 682–687.